

## RESEARCH ARTICLE

10.1002/2017JA023912

This article is a companion to *He et al.* [2017] doi:10.1002/2017JA023913.

## Key Points:

- The largest currently available plasmopause location database is compiled based on observations from 18 satellites from 1977 to 2015
- This database reveals the responses of the global plasmopause locations to solar wind and geomagnetic changes
- The plasmopause locations exhibit clear MLT-dependent diurnal, seasonal, and solar cycle variations

## Supporting Information:

- Supporting Information S1
- Data S1
- Data S2

## Correspondence to:

F. He,  
hefei@mail.iggcas.ac.cn

## Citation:

Zhang, X.-X., F. He, R.-L. Lin, M.-C. Fok, R. M. Katus, M. W. Liemohn, D. L. Gallagher, and S. Nakano (2017), A new solar wind-driven global dynamic plasmopause model: 1. Database and statistics, *J. Geophys. Res. Space Physics*, 122, 7153–7171, doi:10.1002/2017JA023912.

Received 17 JAN 2017

Accepted 14 JUN 2017

Accepted article online 21 JUN 2017

Published online 6 JUL 2017

## A new solar wind-driven global dynamic plasmopause model: 1. Database and statistics

Xiao-Xin Zhang<sup>1</sup> , Fei He<sup>2</sup> , Rui-Lin Lin<sup>3</sup>, Mei-Ching Fok<sup>4</sup> , Roxanne M. Katus<sup>5</sup>, Michael W. Liemohn<sup>6</sup> , Dennis L. Gallagher<sup>7</sup> , and Shinya Nakano<sup>8</sup>

<sup>1</sup>Key Laboratory of Space Weather, National Center for Space Weather, China Meteorological Administration, Beijing, China, <sup>2</sup>Key Laboratory of Earth and Planetary Physics, Institute of Geology and Geophysics, Chinese Academy of Sciences, Beijing, China, <sup>3</sup>National Space Science Center, Chinese Academy of Sciences, Beijing, China, <sup>4</sup>NASA Goddard Space Flight Center, Greenbelt, Maryland, USA, <sup>5</sup>Department of Mathematics, Eastern Michigan University, Ypsilanti, Michigan, USA, <sup>6</sup>Department of Climate and Space Sciences and Engineering, University of Michigan, Ann Arbor, Michigan, USA, <sup>7</sup>NASA Marshall Space Flight Center, Huntsville, Alabama, USA, <sup>8</sup>Institute of Statistical Mathematics, Tachikawa, Japan

**Abstract** A large database, possibly the largest plasmopause location database, with 49,119 plasmopause crossing events from the in situ observations and 3957 plasmopause profiles (corresponding to 48,899 plasmopause locations in 1 h magnetic local time (MLT) intervals) from optical remote sensing from 1977 to 2015 by 18 satellites is compiled. The responses of the global plasmopause to solar wind and geomagnetic changes and the diurnal, seasonal, solar cycle variations of the plasmopause are investigated based on this database. It is found that the plasmopause shrinks toward the Earth globally and a clear bulge appears in the afternoon to premidnight MLT sector as the solar wind or geomagnetic conditions change from quiet to disturbed. The bulge is clearer during storm times or southward interplanetary magnetic field. The diurnal variations of the plasmopause are most probably the result of the difference between the magnetic dipole tilt and the Earth's spin axis. The seasonal variations of the plasmopause are characterized by equinox valleys and solstice peaks. It is also found that the plasmopause approaches the Earth during high solar activity and expands outward during low solar activity. This database will help us study and understand the evolution properties of the plasmopause shape and the interaction processes of the plasmasphere, the ring current, and the radiation belts in the magnetosphere.

### 1. Introduction

The plasmasphere is a torus of cold ( $\sim 1$  eV) and dense (electron density of the order of  $100\text{--}10,000\text{ cm}^{-3}$ ) plasma region surrounding the Earth with the ionospheric originated electrons and ions all trapped on geomagnetic field lines [Lemaire and Gringauz, 1998; Sandel et al., 2003; Kotova, 2007; Darrouzet et al., 2009]. The plasmopause, the outer boundary of the plasmasphere, is often defined as a transition region in which the plasma density usually exhibits a drop of at least half an order of magnitude in less than one Earth radius ( $R_E$ ,  $1 R_E = 6378.0$  km) of altitude [Carpenter, 1963, 1966; Gringauz, 1963; Carpenter and Anderson, 1992]. Since the cold plasma in the plasmasphere is primarily subject to  $\mathbf{E} \times \mathbf{B}$  drift, the plasmopause position is essential in the determination of the inner magnetospheric convections, and it is usually located at geocentric distances of  $3.0\text{--}6.0 R_E$  on the geomagnetic equatorial plane [Lemaire and Gringauz, 1998]. The location of the plasmopause reveals the important interactions of the plasmasphere with the magnetospheric convection and responds to changes in the strength of geomagnetic activity in the inner magnetosphere [e.g., Goldstein et al., 2003a]. It is inferred from several reviews [e.g., Ganguli et al., 2000; Liemohn, 2006; Kotova, 2007; Darrouzet et al., 2009; Pierrard et al., 2009] that the dynamic location of the plasmopause may contribute to the particle precipitation and/or loss (due to wave-particle interaction) of the ring current and the radiation belts, since the plasmasphere, the ring current, and the radiation belts are overlapped in the magnetosphere [Carpenter and Anderson, 1992; Carpenter, 1995; Fok et al., 1995; Khazanov and Liemohn, 1995; Goldstein et al., 2003a; Spasojević et al., 2003].

In the past four decades, many types of instruments have been launched into space to characterize the plasmaspheric density structures and dynamics through in situ measurements and remote sensing [Carpenter, 2004; Goldstein, 2006; Gallagher and Comfort, 2016]. Typical instruments are summarized as follows.

1. *Mass spectrometer.* Measurements of the positive ion concentration by ion traps on Russian satellites in 1950–1959 were the first to discover the plasmasphere and its outer boundary at  $4 R_E$  [Gringauz, 1963; Lemaire and Gringauz, 1998, and references therein]. Chappell *et al.* [1970] and Harris *et al.* [1970] studied the influence of magnetic activity on the plasmopause locations using the measurements from the light ion mass spectrometer aboard OGO 5 [Harris and Sharp, 1969]. Other examples include the retarding ion mass spectrometer on Dynamics Explorer 1 (DE 1), which also provided many in situ measurements of plasmaspheric ion composition and structure [e.g., Comfort *et al.*, 1985; Olsen *et al.*, 1987; Newberry *et al.*, 1989], and the low-energy plasma instruments on the Van Allen Probes that have provided useful data for plasmaspheric studies [e.g., Sarno-Smith *et al.*, 2016].
2. *Plasma wave instruments.* The electron density profiles deduced from the sweep frequency receiver (SFR) measurements on the International Sun-Earth Explorer (ISEE 1) [Ogilvie *et al.*, 1977] were used to develop the first empirical model of the equatorial electron density in the magnetosphere [Carpenter and Anderson, 1992]. From the 1980s on, many plasma wave instruments were used to measure the electron density of the plasmasphere, such as those aboard DE 1 [Shawhan *et al.*, 1981], the Exosphere D satellite (EXOS-D, also known as Akebono) [Tsuruda and Oya, 1991], the Combined Release and Radiation Effects Satellite (CRRES) [Anderson *et al.*, 1992], the Polar satellite [Gurnett *et al.*, 1995], the Imager for Magnetosphere-to-Auroral Global Exploration (IMAGE) [Burch, 2000], the Cluster [Décréau *et al.*, 1997], and the Van Allen Probes (VAP) [Kletzing *et al.*, 2013]. Measurements by these plasma wave experiments have greatly advanced our understanding on the dynamics of the plasmasphere (and the plasmopause).
3. *Optical remote sensing.* The extreme ultraviolet imager (EUV) aboard the IMAGE mission [Sandel *et al.*, 2000] provided for the first time the global EUV images of plasmaspheric  $\text{He}^+$  from polar perspectives for studying the global structures of the plasmasphere. The telescope of extreme ultraviolet (TEX) aboard the Selenological and Engineering Explorer (SELENE) (also known as KAGUYA) [Yoshikawa *et al.*, 2008] launched in 2008 and the EUV Camera (EUVC) aboard the Chang'e-3 mission [Chen *et al.*, 2014] launched in 2013 provided the global EUV images of plasmasphere  $\text{He}^+$  from the side perspective. In the plasmaspheric EUV images, the plasmopause was identified as the outermost sharp edge where the intensity of the 30.4 nm emissions drops abruptly [Goldstein *et al.*, 2003a; He *et al.*, 2016].
4. *Electrostatic analyzer.* The Time History of Events and Macroscale Interactions during Substorms (THEMIS) launched in 2007 provided the total electron density from spacecraft potential and electron thermal velocity [Angelopoulos, 2008], from which several plasmopause models were constructed [Cho *et al.*, 2015; Liu *et al.*, 2015; Verbanac *et al.*, 2015]. This has also been done with the magnetospheric plasma analyzer (MPA) instrument on the geosynchronously orbiting spacecraft operated by the Los Alamos National Laboratory [e.g., Moldwin *et al.*, 1995; Lawrence *et al.*, 1999].

Numerous studies have demonstrated that the shape and geocentric distance of the plasmopause are highly dependent on the geomagnetic and solar wind conditions [e.g., Chappell *et al.*, 1970; Grebowsky, 1970; Horwitz *et al.*, 1990; Carpenter and Anderson, 1992; Moldwin *et al.*, 2002; O'Brien and Moldwin, 2003; Goldstein *et al.*, 2003b, 2005; Gallagher *et al.*, 2005; Larsen *et al.*, 2007; Cho *et al.*, 2015; Liu *et al.*, 2015; Verbanac *et al.*, 2015; Katus *et al.*, 2015; Bandić *et al.*, 2016]. Based on the correlations of the plasmopause with geomagnetic indices such as  $K_p$ ,  $Dst$ , and  $AE$  and solar wind parameters such as the  $z$  component of the interplanetary magnetic field (IMF  $B_z$ ), the solar wind speed, and some energy coupling functions, several empirical or statistical models of the plasmopause locations have been developed. For example, Carpenter and Anderson [1992] derived the well-known  $K_p$ -dependent plasmopause location model using ISEE 1 data. Moldwin *et al.* [2002] and O'Brien and Moldwin [2003] built empirical models of the plasmopause locations as functions of the most recent maximum in  $AE$  or minimum in  $Dst$  based on a database of CRRES observations. Larsen *et al.* [2007] obtained the plasmopause location model as a function of IMF  $B_z$ , IMF clock angle ( $\theta$ ), and a merging proxy (the Kan-Lee electric field,  $\phi = vB^2 \sin^2(\theta/2)$ ) using the IMAGE EUV images. Cho *et al.* [2015] constructed a plasmopause model as a function of IMF  $B_z$ , solar wind flow speed, and  $AE$  based on THEMIS observations, and Liu *et al.* [2015] used the same observation data to establish a magnetic local time (MLT)-dependent dynamic plasmopause location model characterized by the  $SYM-H$ ,  $AL$ ,  $AU$ ,  $AE$ , and  $K_p$  indices. It is noted that the above mentioned plasmopause location models were built based on limited periods of data. The MLT dependence was not included in some of these models because of the limited coverage of the database. The MLT-dependent diurnal, seasonal, and solar cycle variations of the plasmopause have not been fully addressed in these models.

**Table 1.** Satellite Instruments and Data Intervals Used to Extract the Plasmapause Locations

Satellites	Events Number	Instruments	Data Interval
ISEE 1	1080	PWI	13 November 1977 to 21 September 1987
DE 1	1205	PWI	16 September 1981 to 20 June 1984
Akebono	11104	PWS	5 March 1989 to 30 August 1998
CRRES	1165	PWE	1 August 1990 to 10 November 1991
Polar	7223	PWI, EFI <sup>b</sup>	16 March 1996 to 19 December 2006
IMAGE	2584	RPI	1 January 2001 to 18 December 2005
IMAGE	3579 <sup>a</sup>	EUV	13 May 2000 to 31 December 2002
Cluster (1, 2, 3, 4)	6955	WHISPER	2 February 2002 to 31 December 2012
THEMIS (A, D, E)	12024	EFI, ESA	1 January 2008 to 31 December 2015
THEMIS B	177	EFI, ESA	2 July 2008 to 2 December 2009
THEMIS C	602	EFI, ESA	30 June 2008 to 24 March 2010
VAP (A, B)	5000	EMFISIS	1 September 2012 to 31 December 2015
CE 3	378 <sup>a</sup>	EUVC	24 December 2013 to 21 April 2014

<sup>a</sup>These values represent the number of EUV or EUVC images. Each EUV image corresponds to a plasmapause profile with 1 h MLT intervals with full MLT coverage not guaranteed.

<sup>b</sup>The data coverage for PWI is from 2 February 1996 to 16 September 1997, and the data coverage for EFI is from 20 March 1996 to 28 April 2008. For the period before 16 September 1997, the PWI data are used to determine the plasmapause, and the EFI data are used for the period after then. Only data before 2006 are used.

In this paper, a large plasmapause locations database covering the observations from 1977 to 2015 has been compiled to study the global variations of plasmapause locations in different timescales with different geomagnetic indices and solar wind and IMF parameters. A new solar wind-driven global dynamic plasmapause model will be developed based on statistical investigations of the database and will be presented in the companion paper [He et al., 2017]. The outline of the paper is as follows. The observation data, plasmapause extraction methods, and the establishment of the large plasmapause database are introduced in detail in section 2. The statistical analysis of the global shape variations and the MLT-dependent diurnal, seasonal, and solar cycle variations of the plasmapause will be presented in section 3. A summary and conclusion will be given in section 4.

## 2. Data and Methodology

### 2.1. Overview of Data

In this investigation, there are two kinds of plasmapause location data obtained from different instruments aboard different satellites listed in Table 1. Among these data, 49,119 plasmapause crossings have been

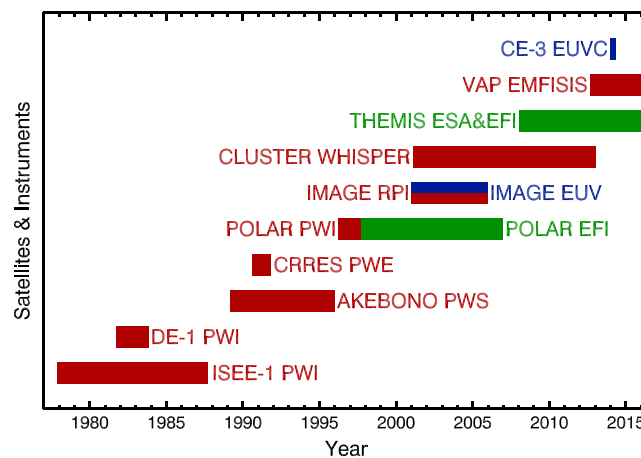


**Figure 1.** Coverages and overlap of satellite data used in this paper. The plasmaspheric observing instruments on board these satellites can be divided into three categories of plasma wave instruments (red), optical remote sensing instruments (blue), and electrostatic analyzers (green).

extracted from the in situ plasma wave instruments, e.g., the Plasma Wave Investigation (PWI) on ISEE 1 [Ogilvie et al., 1977; Gurnett et al., 1978], the Plasma Wave and Quasi-Static Electric Field Instrument (PWI) on DE 1 [Shawhan et al., 1981; Gurnett and Inan, 1988], the Plasma Wave Observation and Sounder Experiments (PWS) on Akebono [Tsuruda and Oya, 1991; Oya et al., 1990], the Plasma Wave Experiment (PWE) on CRRES [Anderson et al., 1992], the Plasma Wave Instrument (PWI) and Electric Field Instrument (EFI) on Polar [Gurnett et al., 1995; Harvey et al., 1995], the Radio Plasma Imager (RPI) [Reinisch et al., 2000] on IMAGE [Burch, 2000], the Waves of High frequency and

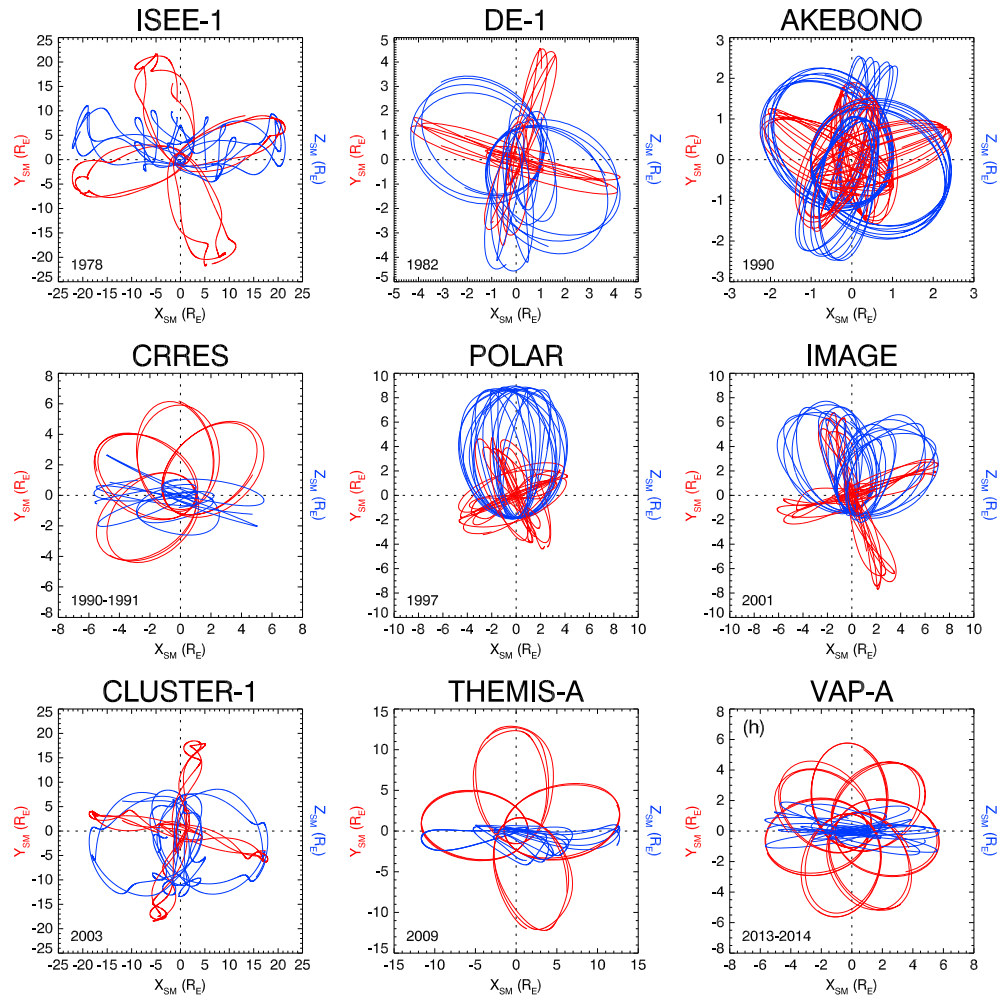


**Figure 2.** Sampled orbits of the nine Earth-orbiting satellites in the  $xy$  plane (red curves) and  $xz$  plane (blue curves) in the SM coordinate system. For multisatellite missions of Cluster (four satellites), THEMIS (five satellites), and VAP (two satellites), only one of each is plotted.

Sounder for Probing of Electron density by Relaxation (WHISPER) on Cluster [D  cr  au *et al.*, 1997; Darrouzet *et al.*, 2002], the Electric Field Instrument (EFI) and the Electrostatic Analyzer (ESA) on THEMIS [McFadden *et al.*, 2008; Bonnell *et al.*, 2008], and the Electric and Magnetic Field Instrument Suite and Integrated Science (EMFISIS) on VAP [Kletzing *et al.*, 2013; Kurth *et al.*, 2015].

Based on the plasmaspheric images observed by the IMAGE EUV imager [Sandel *et al.*, 2000] and the CE 3 EUVC instrument [Chen *et al.*, 2014; He *et al.*, 2016], the plasmopause locations on the magnetic equatorial plane were reconstructed with the Minimum L Algorithm (MLA, see Appendix A). In total, 3579 and 378 plasmaspheric images were selected from IMAGE EUV from 2000 to 2002 and from CE 3 EUVC in 2014, respectively, and 48,899 plasmopause locations were obtained in 1 h MLT intervals.

The data intervals, satellite names, and instruments for these available plasmaspheric observations are listed in Table 1 and are also shown in Figure 1. The orbits of these satellites corresponding to Table 1 are plotted in Figure 2 (only the trajectories around the beginning, the first quarter, the middle, and the third quarters of an orbital regression cycle are plotted). The orbital regression cycle of CRRES and VAP is approximately 2 years, and that of the other satellites except CE 3 is 1 year, making all of magnetic local time (MLT) sampled. It is noted that the CE 3 lunar lander is on the lunar surface ( $\sim 60 R_E$  away from the Earth), and the plasmaspheric images from EUVC were only obtained in the magnetic local time (MLT) sector between 4.0 h and 6.0 h [He *et al.*, 2016].

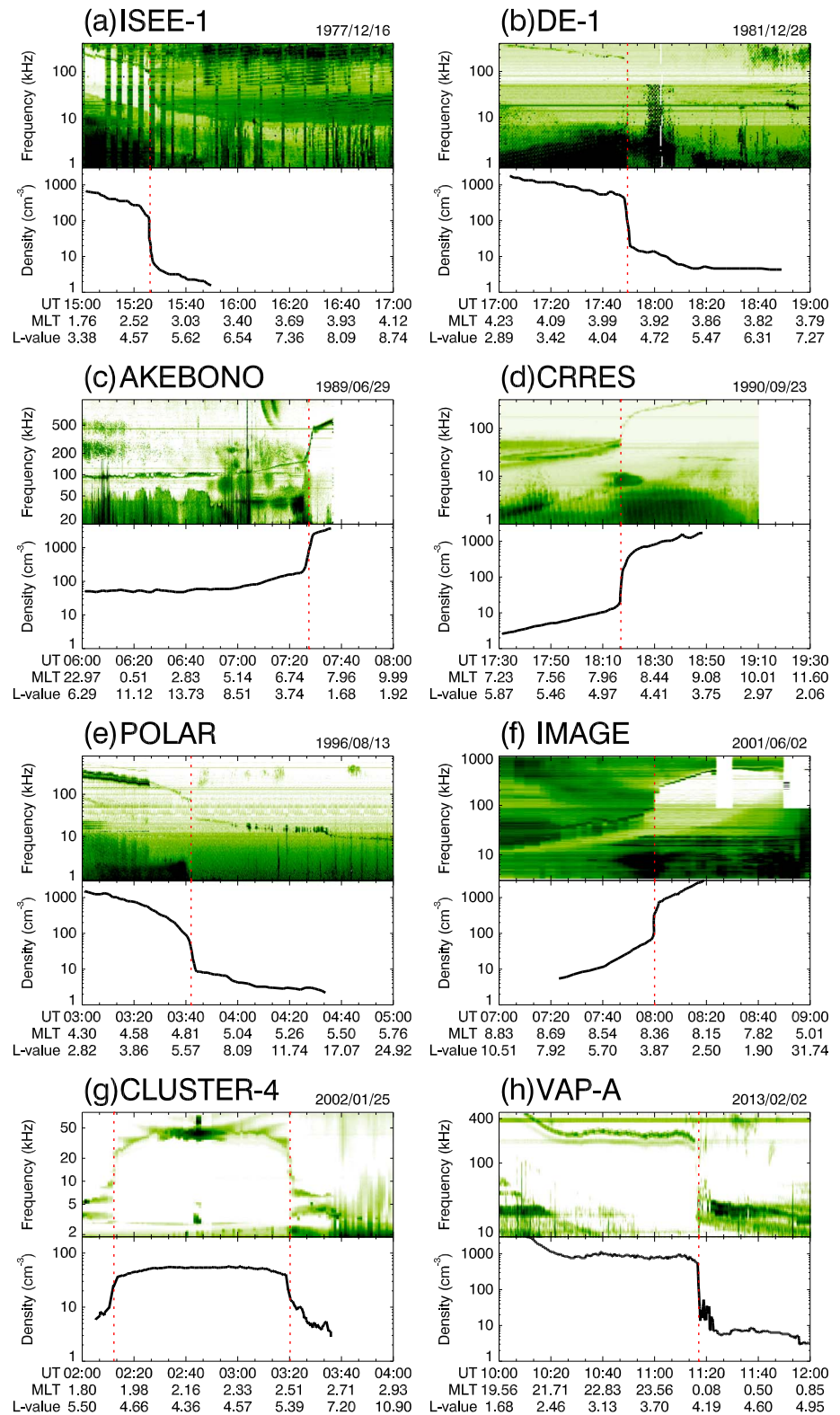


**Figure 3.** Examples of the spectrograms of the eight plasma wave instruments showing the UHR band and plasmopause crossings. The electron densities deduced from the UHR frequencies are shown in the bottom of each panel. Red vertical dashed lines in each panel represent the plasmopause crossings.

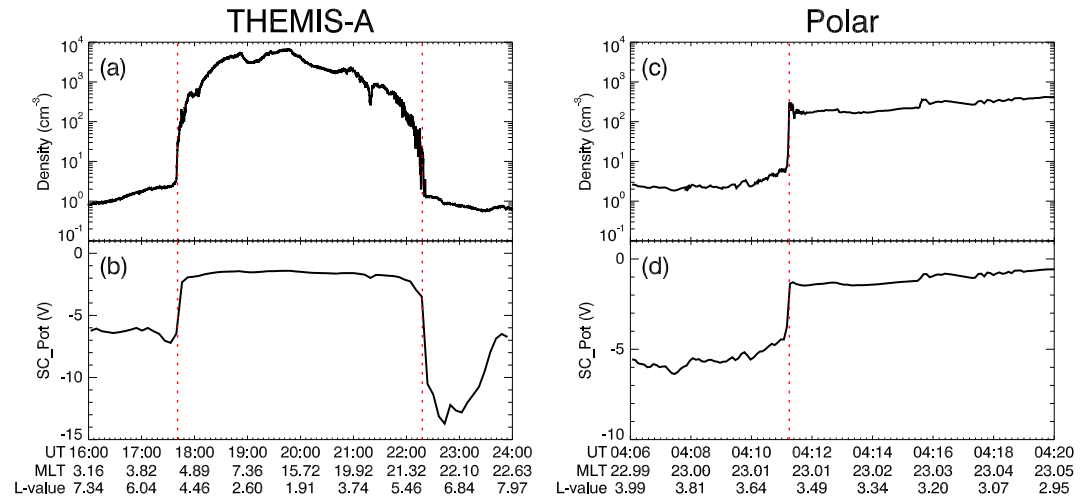


**Figure 4.** The spacecraft potential and electron density measured by (a, b) THEMIS A on 31 March 2010 and (c, d) Polar on 25 April 1998, respectively. Red vertical dashed lines represent the identified plasmopause locations.

All the data were obtained during the period from November 1977 to December 2015 (more than 38 years), covering almost four solar cycles (21, 22, 23, and 24). The plasmaspheric observations in this investigation include two types; one is the in situ measurements (plasma wave instruments and electrostatic analyzers), and the other is from optical remote sensing. The detailed plasmopause determination criteria for the plasmaspheric observations will be described in detail in the following sections.

### 2.2. Plasmopause Determination From In Situ Crossings

For the plasma wave instruments (ISEE 1 PWI, DE 1 PWI, Akebono PWS, CRRES PWE, Polar PWI, IMAGE RPI, Cluster WHISPER, and VAP EMFISIS), a typical signature in the frequency-time spectrograms is the upper hybrid resonance (UHR) frequency ( $f_{UHR}$ , in Hz). The electron density ( $n_e$ , in  $\text{cm}^{-3}$ ) can be related to  $f_{UHR}$  through the following formula [Kurth et al., 2015]:

$$n_e = \frac{f_{UHR}^2 - f_{ce}^2}{8980^2} \quad (1)$$

where  $f_{ce} = eB/m_e$  is the electron cyclotron frequency,  $B$  is the strength of the magnetic field in nanotesla,  $e$  is the electron charge, and  $m_e$  is the electron mass. Here  $f_{ce}$  is estimated with the International Geomagnetic Reference Field (IGRF) internal magnetic field model combined with the Tsyganenko 2007 external magnetic field model [Tsyganenko and Sitnov, 2007; Sitnov et al., 2008] since not all the satellites are equipped with a scientific magnetometer. This method of deducing electron densities has been successfully applied to all the plasma wave instruments in many studies [Oya et al., 1990; Moldwin et al., 2002; Goldstein et al., 2003a; Darrouzet et al., 2004; Kurth et al., 2015; and references therein] with an accuracy close to 10% [Goldstein et al., 2014; Kurth et al., 2015]. Examples of the frequency-time spectrograms of the in situ plasma wave environment and the electron densities deduced from  $f_{UHR}$  are shown in Figure 3.

For the THEMIS satellites, the spacecraft potential (refers to the potential of the spacecraft body relative to the ambient plasma) measured by the EFI and the electron thermal velocities measured by the ESA are used to calculate the electron density with the detailed method described in Mozer [1973] and Pedersen et al. [1998]. The calculated electron densities are associated with an error of a factor of 2, which is smaller than the density drop around the plasmopause, and have been widely used to identify the plasmopause locations [Li et al., 2010; Cho et al., 2015; Liu et al., 2015]. An example of the electron density profile and corresponding satellite potential is shown in Figures 4a and 4b.

For the Polar satellite, the electron densities inferred from the spacecraft potential measured by EFI [Scudder et al., 2000; Kim et al., 2010] were used to determine the plasmopause locations after 16 September 1997 when the PWI data were unavailable. An example of the electron density profile and corresponding satellite potential is shown in Figures 4c and 4d.

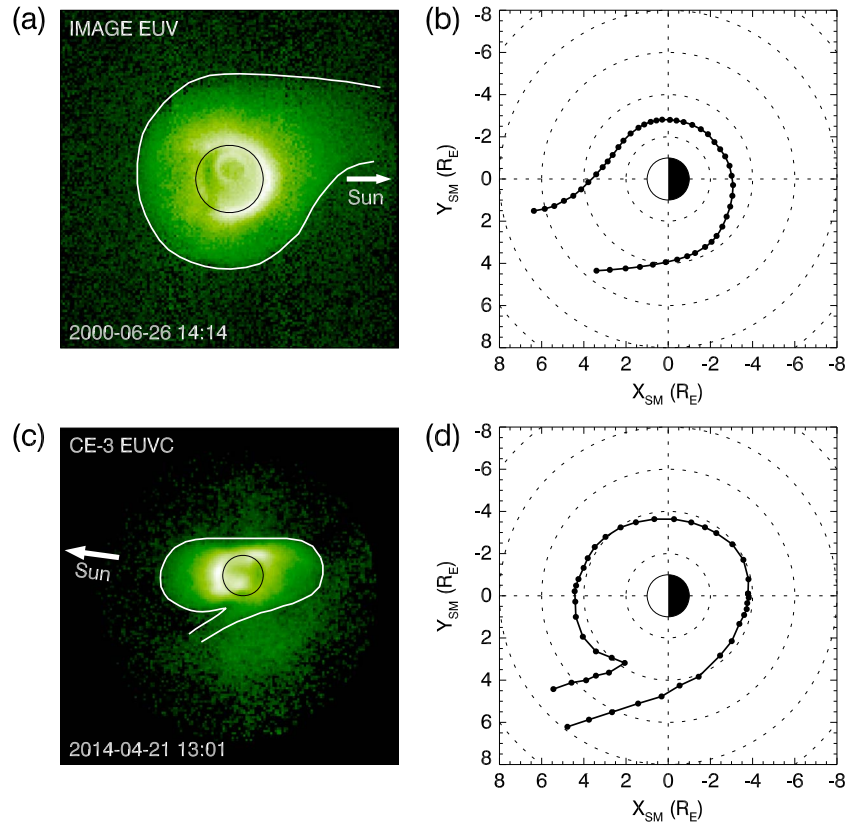


**Figure 5.** Examples of plasmopause determinations from EUV images. (a and c) EUV images with the manually extracted plasmopause outlines shown by white curves. (b and d) Extracted plasmopause locations shown by solid and dotted lines from EUV images on the magnetic equator via MLA.

As widely adopted in previous studies [Carpenter and Anderson, 1992; Moldwin et al., 2002; Darrouzet et al., 2013; Cho et al., 2015; Kwon et al., 2015; Liu et al., 2015], a density drop of a factor of 5 or more over an  $L$  distance smaller than 0.5 is required for a plasmopause crossing. This criterion is also adopted in this investigation. Finally, the plasmopause locations identified from the deduced electron density profiles are shown by the vertical red dashed lines in Figures 3 and 4.

### 2.3. Plasmopause Determination From Optical Imagers

For the EUV imaging instruments on board IMAGE and CE 3, various techniques [Roelof and Skinner, 2000; Sandel et al., 2003; Wang et al., 2006, 2007; He et al., 2011, 2012, 2016] have been developed to interpret the plasmopause locations. In this investigation, the MLA technique [Wang et al., 2007; He et al., 2011, 2016] is used to determine the plasmopause locations from the EUV images. In the EUV images, each pixel corresponds to a line of sight (LOS) integration of the resonantly scattered sunlight at 30.4 nm with the emission intensity proportional to the column integrated density of  $\text{He}^+$  along the LOS. A typical signature in a plasmaspheric EUV image is the sharp edge where the brightness of 30.4 nm  $\text{He}^+$  emissions drops abruptly. This sharp edge can reliably be treated as the plasmopause outline [Goldstein et al., 2003a; He et al., 2011, 2016]. For each pixel in the outline boundary, the corresponding LOS is calculated, and all the magnetic field lines intersected by the LOS are traced onto the magnetic equator to get the field line with minimum  $L$  value which is treated as the plasmopause. Different pixels in the outline boundary correspond to different MLTs when traced onto the magnetic equator, and the MLT dependence of the plasmopause location can be finally determined by the MLA. Detailed description of the MLA can be found in the Appendix A and the supporting information. Examples of plasmopause profiles extracted from an IMAGE EUV image obtained at 14:14 UT on 26 June 2000 and a CE 3 EUVC image taken at 13:01 UT on 21 April 2014 are shown in Figure 5. It is noted that only the plasmaspheric EUV images with sharp edges with radial intensity drops of at least 1 order of magnitude are analyzed to ensure the reliability of the results, the MLT

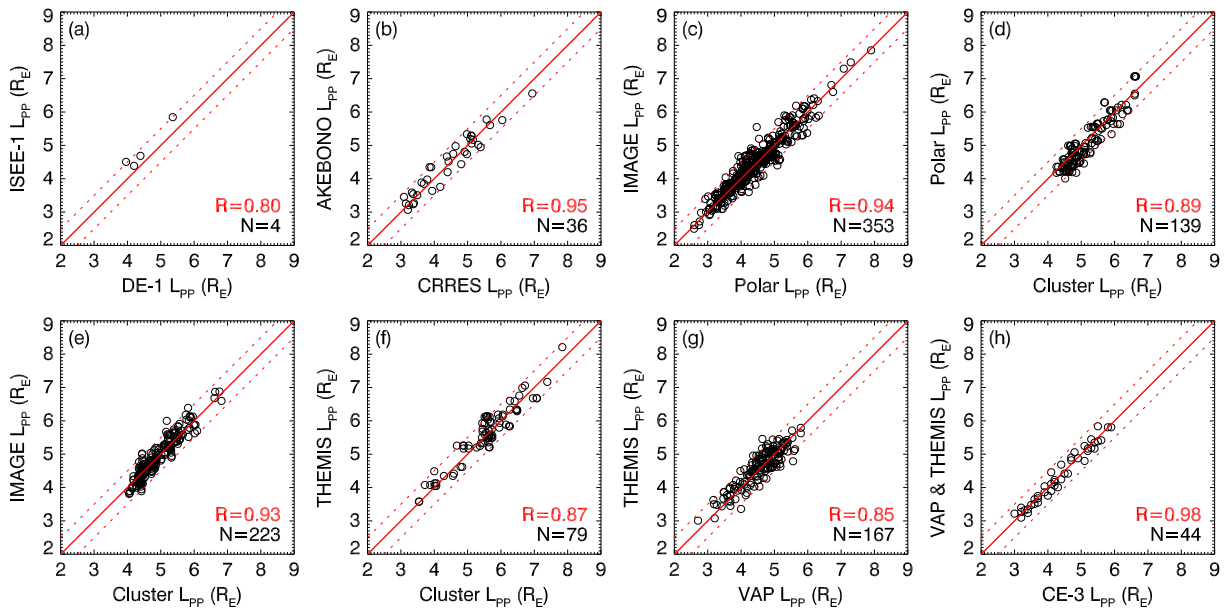


**Figure 6.** Comparisons between plasmopause locations that are simultaneously observed by two different satellites at the same MLTs. Satellites used in the comparison in each panel are labeled as the titles of the corresponding axes, respectively. The red solid and dashed lines indicate perfect agreement and errors of  $\pm 0.5 R_E$ , respectively. Black and red numbers in each panel denote the number of circles and the linear correlation coefficient, respectively.

sectors with multiple plasmapauses are also excluded, and the plasmopause locations determined from EUV or EUVC are resampled into 1.0 h MLT intervals.

#### 2.4. Comparisons Between Different Satellites

To verify the consistency between the plasmopause locations extracted from different satellites with different methods, comparisons between different satellites are conducted. Our purpose is to check whether the plasmopause locations observed by two different satellites at the same UT and same MLT have the same  $L$  values. Due to the orbital differences between different satellites, it is almost impossible to find exact simultaneous plasmopause crossings. Therefore, a time window of 20 min and a MLT window of 1 h are adopted to search the plasmopause locations that are almost simultaneously observed by two satellites. For a plasmopause location observed by satellite A (A can be any satellite listed in Table 1) and parameterized by  $UT_A$ ,  $MLT_A$ , and  $L_A$  (calculation of MLT and  $L$  is introduced in the next section), the plasmopause location parameterized by  $UT_B$ ,  $MLT_B$ , and  $L_B$  observed satellite B (B can be any satellite listed in Table 1 with  $B \neq A$ ) is automatically searched out if  $|UT_A - UT_B| < 20$  min and  $|MLT_A - MLT_B| < 1$  h. For each satellite pair (e.g., A-B), a subdatabase of  $L_A$  and  $L_B$  pairs is established. After all the satellite pairs are processed using the above procedure, eight subdatabases with a total of 1045  $L_A$ - $L_B$  pairs are established as shown in Figure 6. The number of  $L_A$ - $L_B$  pairs in each subdatabase is shown at the lower right corner of each panel in Figure 6.

If the plasmopause locations determined from two different satellites agree perfectly, all the circles would lie along the red solid lines ( $L_A = L_B$ ) in Figure 6. Actually, 95% of the circles are within  $0.5 R_E$  of perfect agreement. The dashed lines in each panel are drawn at  $L_A = L_B \pm 0.5 R_E$  for reference. The linear correlations between  $L_A$  and  $L_B$  are all larger than 0.8 (highly significant) as shown by the red numbers in each panel in Figure 6. This indicates that the plasmopause locations determined from different types of plasmaspheric observations are consistent and our plasmopause determination methods are reasonable and reliable for further statistical investigation and model establishment. Therefore, the resulting error estimated for determining the plasmopause location for each data source is less than  $0.5 R_E$ .

#### 2.5. Plasmopause Location Database Compilation

Using the above introduced methods and criteria, 49,119 plasmopause locations are identified from the in situ observations and 3957 plasmopause profiles (corresponding to 48,899 plasmopause locations in 1 h



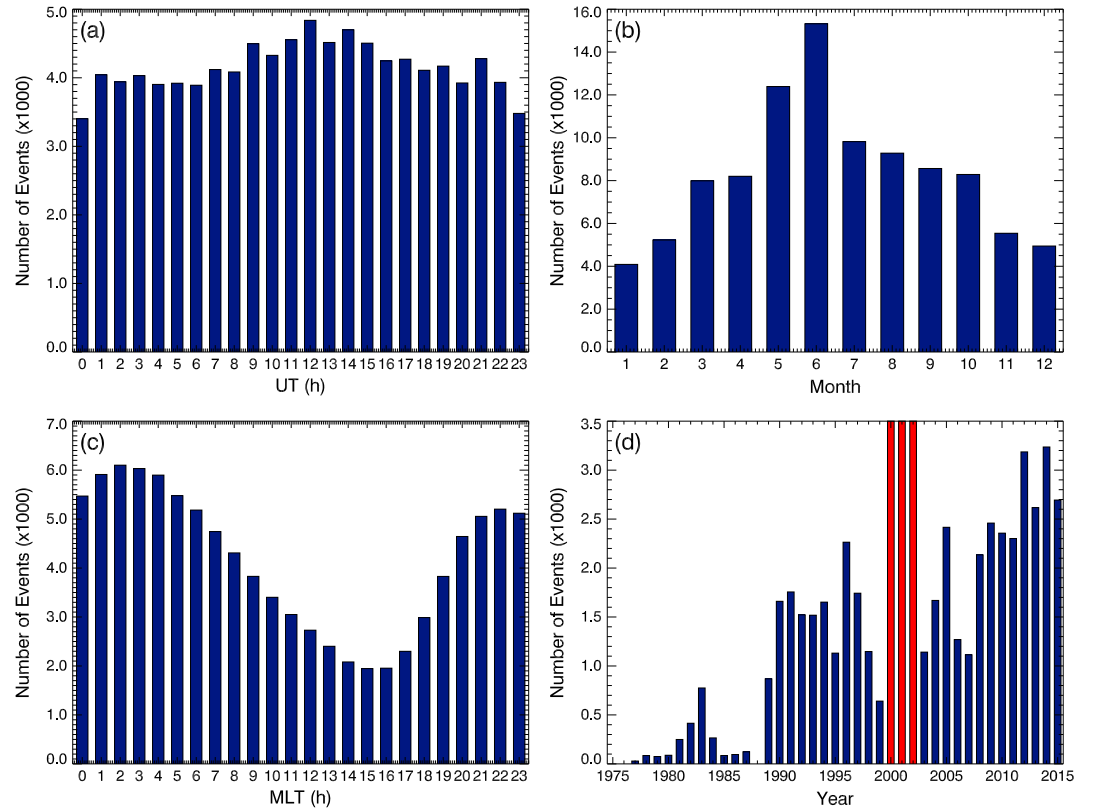


**Figure 7.** Distributions of the plasmapause locations versus (a) UT, (b) month, (c) MLT, and (d) year. The numbers of events for the three red histograms in Figure 7d are 16,163, 24,140, and 12,594, respectively, due to the large number of events from IMAGE EUV.

MLT intervals) are extracted from the EUV images. Since the plasmapause crossings of all the satellites are not all located in the solar magnetospheric (SM) equator, the IGRF internal magnetic field model combined with the Tsyanenko 2007 external magnetic field model are used to map the crossings to the SM equator, and the corresponding UT,  $L$  value ( $L_{pp}$ ), and MLT are stored into a database. Then, all the crossings in the database are matched with the geomagnetic indices of 3 h  $Kp$ , 1 h  $Dst$ , 5 min  $SYM-H$ , and 5 min  $AE$ , as well as the 5 min averaged solar wind speed ( $V_{SW}$ ), solar wind number density ( $N_{SW}$ ),  $y$  component of IMF (IMF  $B_y$ ), and  $z$  component of IMF (IMF  $B_z$ ). The  $Dst$ ,  $SYM-H$ , and  $AE$  indices are provided by the Kyoto World Data Center for Geomagnetism, the  $Kp$  index is provided by the German Research Centre for Geosciences (GFZ), and the solar wind data are obtained from the NASA's CDAWEB OMNI.

In matching the solar wind and IMF parameters, since the OMNI data have been time shifted to the nose of the Earth's bow shock, here we just consider the propagation of the solar wind from the bow shock nose to the high latitude polar region. According to Zhang *et al.* [2005], the time shift includes two parts. The first part is the time delay ( $\tau_{mp}$ ) from the bow shock to the subsolar magnetopause using the average shocked solar wind velocity ( $V_{SWX}$ ) with a reduction factor of 8. The second part is the estimated time ( $\tau_{Alfven}$ ) of Alfvénic perturbation propagating from the subsolar magnetopause to the Earth's high latitude region. The bow shock position  $X_{BS}$  is calculated from the Chao *et al.* [2002] bow shock model, and the subsolar magnetopause position  $X_{MP}$  is obtained by the Lin *et al.* [2010] magnetopause model. The total time shift,  $T_{shift}$ , can be written as

$$\begin{aligned}
 T_{shift} &= \tau_{mp} + \tau_{Alfven}, \\
 \tau_{mp} &= \frac{X_{BS} - X_{MP}}{V_{SWX}} \times 8, \\
 \tau_{Alfven} &= 2.0 \text{ min}.
 \end{aligned} \tag{2}$$

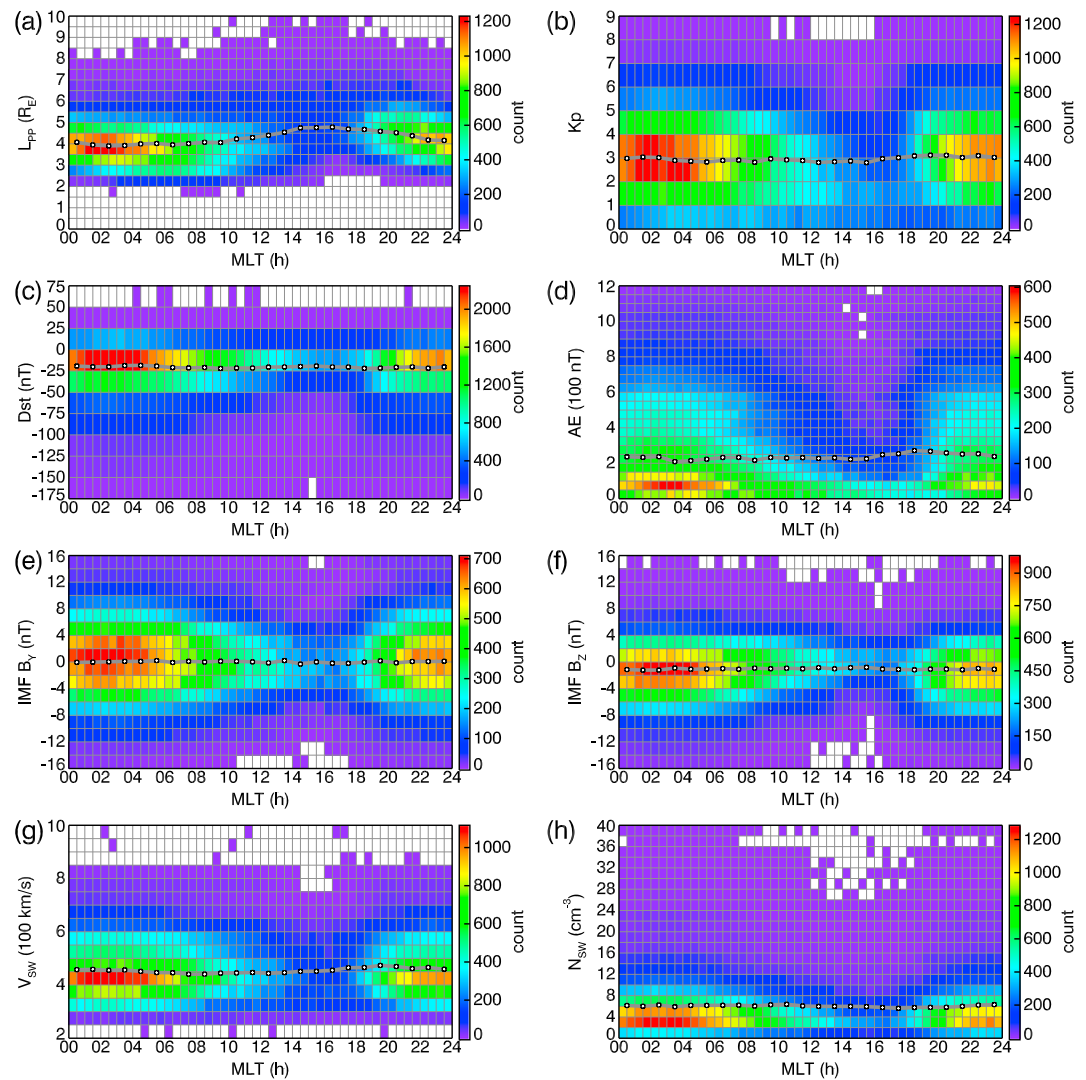


**Figure 8.** MLT distributions (0.5 h bins) of the plasmopause events on (a)  $L$  value (0.5  $R_E$  bins), (b)  $K_p$  index (1.0 bins), (c)  $Dst$  index (25 nT bins), (d)  $AE$  index (50 nT bins), (e)  $IMF B_y$ ,  $y$  component of IMF in GSM coordinate system (2 nT bins), (f)  $IMF B_z$ ,  $z$  component of IMF in GSM coordinate system (2 nT bins), (g)  $V_{sw}$ , solar wind flow speed (50 km/s bins), and (h)  $N_{sw}$ , solar wind density (2.0  $cm^{-3}$  bins). The thick dotted lines in each panel represent average values in 1 h bins. Note that each panel has a different color bar, which is scaled as shown to the right of each panel.

Since the 5 min averaged OMNI data are available only after 1995, only the plasmopause locations observed after 1995 are matched with the shifted solar wind and IMF parameters.

### 2.6. Overview of Database

The histograms of the number of plasmopause locations versus UT, month, MLT, and year are shown in Figure 7. There are more than 3000 events in each 1 h UT bin and more than 4000 events in each month, as shown in Figures 7a and 7b, respectively. It is shown in Figure 7c that there are more than 2000 events in each 1 h MLT bin, providing statistical confidence for establishment of an empirical plasmopause model with MLT dependence. The event numbers in each year are shown in Figure 7d. Due to the low plasmaspheric crossing frequency of ISEE 1, the yearly event number is small before 1987 (except for 1981–1984 when DE 1 data were available) compared with other satellites after 1990. No plasmaspheric observation is found in 1988 (based on our knowledge).

The MLT distributions of the plasmopause locations versus various parameters are shown in Figure 8. Figure 8a reveals that most of the plasmopause locations are observed between 3.0  $R_E$  and 6.0  $R_E$ . A clear bulge

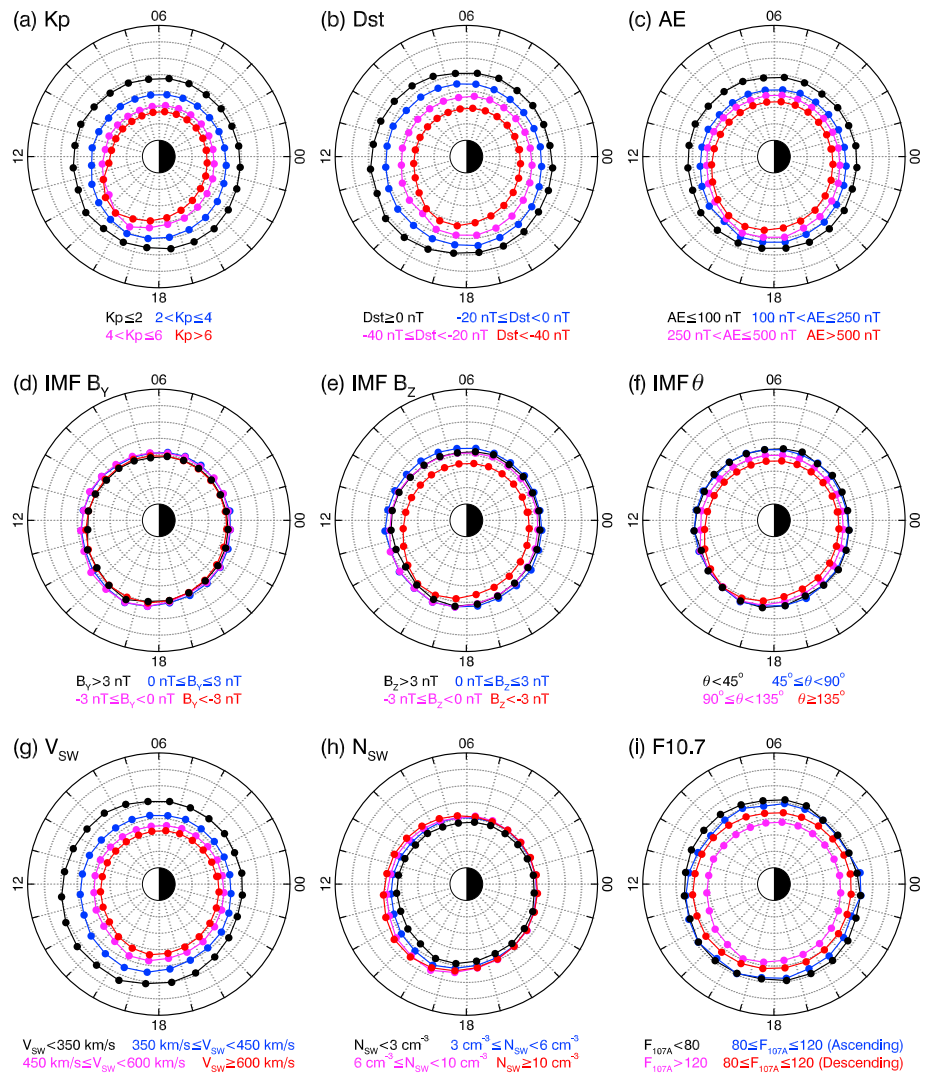


**Figure 9.** Global shapes of the plasmapause for different levels of activity, parameterized by (a)  $K_p$ , (b)  $Dst$ , (c)  $AE$ , (d) IMF  $B_Y$ , (e) IMF  $B_Z$ , (f) IMF clock angle  $\theta$ , (g)  $V_{SW}$ , (h)  $N_{SW}$ , and (i)  $F_{10.7}$ , respectively. The dotted circles are drawn from  $2.0 R_E$  to  $7.0 R_E$  with  $1 R_E$  intervals. The dotted radial lines are drawn in 1 h MLT intervals. Different colors representing different levels of activity are shown at the bottom of each panel.

structure is shown in Figure 8a in the dusk sector as demonstrated by the gray dotted curve. Figures 8b–8d indicate that most of the plasmapause locations are observed during periods of quiet or slightly disturbed geomagnetic conditions, with average  $K_p$  index of  $\sim 3.0$ , average  $Dst$  index of  $\sim -20$  nT, and average  $AE$  index of  $\sim 250$  nT, respectively. For the IMF conditions,  $B_Y$  and  $B_Z$  for most of the plasmapause locations are between  $-10.0$  and  $10.0$  nT with average values of  $B_Y$  around  $0.0$  nT and  $B_Z$  around  $-1.0$  nT as shown in Figures 8e and 8f, respectively. Figures 8g and 8h demonstrate that most of the plasmapause locations are observed when  $V_{SW}$  is less than  $600$  km/s and  $N_{SW}$  is less than  $12.0$   $\text{cm}^{-3}$  with average values of  $\sim 450$  km/s and  $\sim 6.0$   $\text{cm}^{-3}$ , respectively.

### 3. Variations of Plasmapause Locations

Based on the large database covering almost four solar cycles with sufficient sampling of the geomagnetic indices and solar wind and IMF parameters, we could more thoroughly investigate the global shape variations and the MLT-dependent diurnal, seasonal, and solar cycle variations of the plasmapause locations.

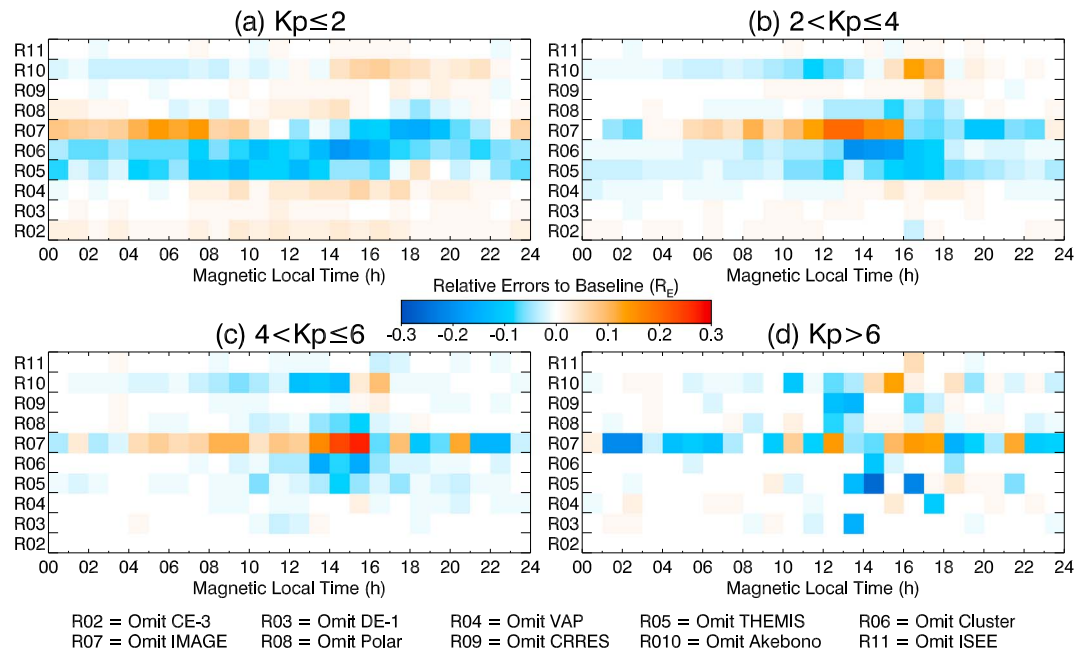


**Figure 10.** Relative errors of R02–R11 to R01 (baseline).

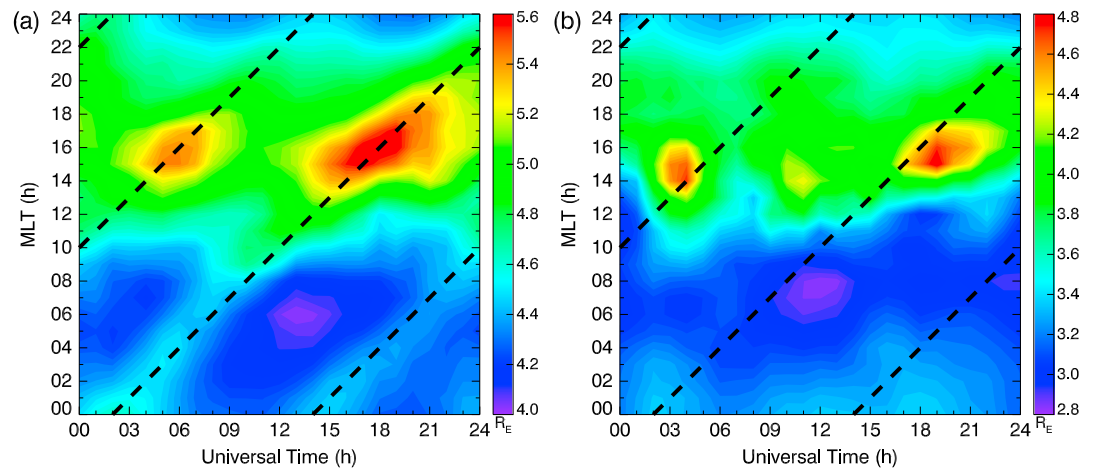
### 3.1. Variations of Global Shape

Figure 9 shows global shapes of the plasmapause under different geomagnetic, solar wind, and IMF conditions. The dotted curves are binned in 1 h MLT intervals. Black, blue, purple, and red lines represent different levels of activity, typically (but not always) lowest to highest, respectively, as demonstrated at the bottom of each panel. In Figure 9, the IMF clock angle  $\theta$  is defined by  $\theta = \text{atan}(|B_Y|/B_Z)$ , with  $\theta = 0^\circ$  for northward IMF and  $\theta = 180^\circ$  for southward IMF. In addition, the solar cycle phase (minimum, ascending, maximum, and descending for the four colors, respectively) is determined by the value and time sequence of  $F_{10.7A}$ , which is the yearly average of the daily  $F_{10.7}$  values. It needs to be noted that  $F_{10.7A}$  must be greater than the previous year's average for the ascending solar cycle phase, while  $F_{10.7A}$  must be less than the previous year's average for the descending solar cycle phase.

The *t* test [Press et al., 1992] shows that the average plasmapause locations at different activity levels are truly different from each other. The curves in Figures 9a–9c and 9g are truly different at all MLT sectors with significance levels of 100%, and the significance levels are generally 95% in Figure 9d (except for the black-red and blue-purple comparisons in almost all MLT sectors), Figure 9e (except for the purple-black comparison in the 6 h to 12 h and 16 h to 20 h MLT regions and the purple-blue comparison in the 13 h to 17 h MLT range), Figure 9f (except for the black-blue comparison in all MLT sectors and all colors between 13 h and 16 h MLT), Figure 9h (except for nightside MLT sectors), and Figure 9i (except for the blue-black comparison in the 12 h to 18 h MLT sector).

To further quantify the uncertainties in the statistical results in Figure 9, the analysis is run for 11 times (R01–R11) for the data binned by *Kp*. R01 is set to be the baseline, in which the plasmapause data from all the 10 missions are included. In each run from R02 to R11, the plasmapause data from one mission are omitted. Here the plasmapause data are also binned into four groups according to *Kp* levels shown in Figure 9a in each run. The relative errors of R02–R11 to R01 for each *Kp* level are shown in Figure 10. It is shown that all the relative errors are less than 0.3  $R_E$ . Based on the comparisons in section 2.4, the *t* test above, and the multiple runs here, it is demonstrated that the database established in this investigation is credible and correct and is suitable for statistical study of the plasmapause locations.

Based on the statistical results in Figure 9, the variations of the global shapes of the plasmapause can be summarized as follows:



**Figure 11.** The contour plot of the diurnal MLT variations of the plasmapause for (a)  $Kp < 4$  and (b)  $Kp \geq 4$ , in  $R_E$  with the color bar shown at the right, respectively. The dashed lines are drawn at slopes of  $dMLT/dUT = 1.0$ , indicating the same shift rate in both MLT and UT (i.e., perfect corotation).

1. As the geomagnetic, solar wind and IMF conditions change from quiet to disturbed, the plasmapause shrinks toward the Earth at all MLTs, except for changes in  $B_Y$  shown in Figure 9d and increases in  $N_{SW}$  in Figure 8h. Increasing  $N_{SW}$  results in the outward expansion of the plasmapause in Figure 9h. The possible reason for this phenomenon may be that  $N_{SW}$  is generally inversely proportional to  $V_{SW}$  [Russell, 2001] and the corresponding geomagnetic activity is relatively weak for large  $N_{SW}$ .
2. A significant plasmaspheric bulge is shown in the afternoon to premidnight MLT sector in all panels of Figure 9 under all levels of activities. The bulges are more significant under disturbed periods (purple dotted and red dotted lines). This feature is consistent with the traditional picture for large-scale plasmaspheric convection [Chen and Wolf, 1972; Rasmussen et al., 1993]. This may also be caused by the fact that plasmaspheric plumes are observed mostly during disturbed periods, e.g., storm times or southward IMF (such as shown in Darrouzet et al. [2008]).
3. The shape of the plasmapause is found to be significantly different between active and quiet conditions. Generally, the differences between the storm time (red dotted lines in Figures 9a and 9b) and non-storm time (black dotted lines in Figures 9a and 9b) plasmapause locations can be larger than  $2.5 R_E$  in equatorial geocentric distance and the decrease in plasmapause locations can be as large as  $2.0 R_E$  during substorm times (red dotted line in Figure 9c).
4. Orientation of the IMF can also change the plasmapause shape. The plasmapause shapes have little variation for different conditions of IMF  $B_Y$  (Figure 9d). The plasmapause locations move inward significantly when  $B_Z < -3$  nT (Figure 8e). Figure 9f further reveals that southward IMF (black dotted and blue dotted lines) can cause obvious shrinkage of the plasmapause which has little change during northward IMF (purple dotted and red dotted lines). Detailed correlations of the plasmapause locations with the solar wind and IMF parameters will be discussed elsewhere [He et al., 2017].
5. Clear solar cycle variations are shown in Figure 9i. The plasmapause is the farthest from the Earth during solar minimum (black dotted line), then moves toward the Earth during the solar ascending phase (blue dotted line) and is the closest to the Earth during solar maximum (purple dotted line) followed by an outward expansion during the solar descending phase (red dotted line).

### 3.2. Diurnal Variations

Figure 11 presents the diurnal variations of the plasmapause locations under geomagnetically quiet ( $Kp < 4$ ) and disturbed ( $Kp \geq 4$ ) conditions. It is worth recognizing that  $Kp = 3$  to 4 represents moderately disturbed conditions and  $Kp$  alone does not discriminate between quiet and disturbed plasmaspheric distributions.  $Kp$  could be in this range, yet has most recently been in a state of prolonged quiet, prolonged activity, or prolonged variability. Each of these generalized conditions will result in distinct distributions of plasmaspheric plasma. This is a systemic limitation of all the geomagnetic indices. It is acknowledged that these interpretations of the statistical data are somewhat compromised in this way. The plasmapause locations are first

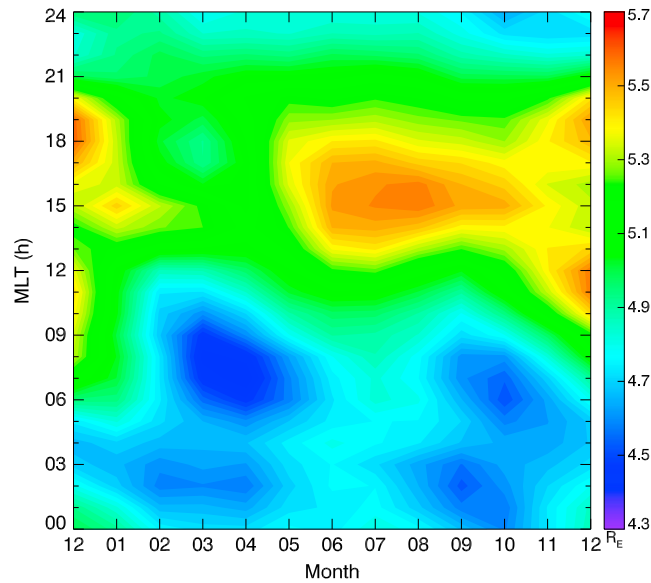


**Figure 12.** The contour plot of the seasonal MLT variations of the plasma-pause in  $R_E$  with the color bar shown at the right.

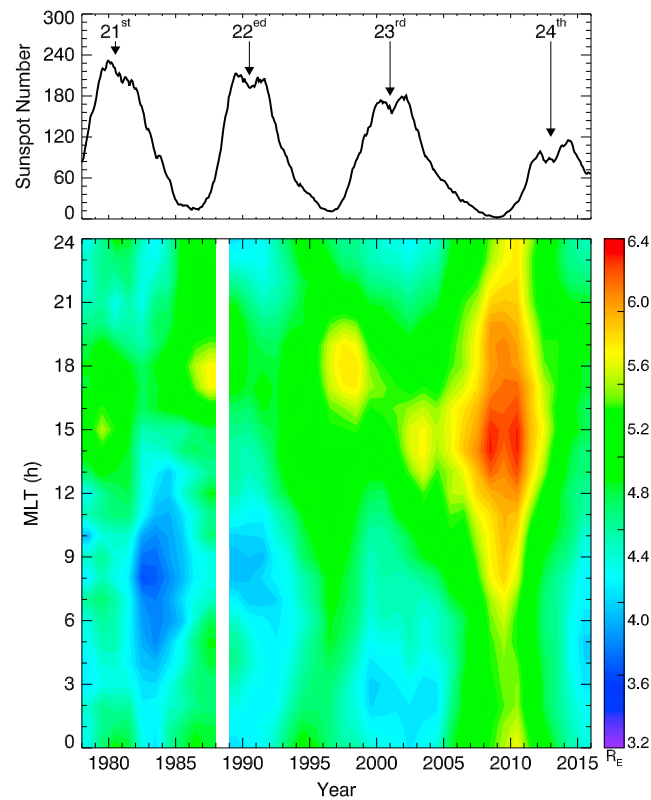


**Figure 13.** (top) Plot of the monthly averaged sunspot numbers for solar cycles 21–24 as marked by the vertical arrows. (bottom) The contour plot of the yearly MLT variations of the plasma-pause, in  $R_E$ , with the color bar shown at the right.

binned into an MLT-UT coordinate frame in 1 h intervals and then plotted in Figure 11. The plasma-pause locations in the 12 h to 21 h MLT sector are generally greater than at other MLT, consistent with the average curve in Figure 8a, possibly because the plasmaspheric bulges or plumes are mostly observed in the afternoon to the premidnight MLT sectors [Darrouzet et al., 2008].

Figure 11 also reveals that there is a strong correlation with UT, which represents both time and geographic longitude. This is independent of season and only loosely dependent on geomagnetic activity. The double peaks around 16 h MLT are most probably the result of the difference between the magnetic dipole tilt and the Earth’s spin axis. The North Geographic Pole is about 4.7 h west of Greenwich. The large peaks best match that offset for quiet conditions in Figure 11a but are shifted for active conditions in Figure 11b, both shifted toward midnight slightly. Inside of  $L$  value =  $4.5 R_E$  ( $\sim 0$  h – 9 h MLT) there is a local maximum in the plasma-pause radius at 2 times of the day. The peak near 0 h MLT and 2 h UT shifts to later MLT faster than UT (the dashed lines indicate the shifts at the same rate of MLT and UT, that is  $dMLT/dUT = 1.0$ ). The other peak shifts at about the same rate in MLT and UT. The peaks near 16 h MLT also shift differently relative to UT, possibly due to the fact when the solar wind or geomagnetic condition becomes disturbed, the strong convection electric fields dominate the dynamics of the plasmasphere [Carpenter and Park, 1973; Katus et al., 2015]. Figure 11 exhibits a statistical picture of the plasma-pause azimuthal shape modulated by the magnetic dipole tilt. That how much of this display is

influenced by the degree of corotation [Sandel et al., 2003; Burch et al., 2004; Gallagher et al., 2005] and how much by geography [Menk et al., 2012] needs further refined investigations.

### 3.3. Seasonal Variations

The seasonal variations of the plasmopause locations are shown in Figure 12. The seasonal variation of the plasmopause is characterized by obvious valleys in equinoxes and peaks in solstices in Figure 12. This seasonal variation seems to be the result of the Russell-McPherron effect [Russell and McPherron, 1973]. According to the Russell-McPherron effect, geomagnetic activity is strong during equinoxes and weak during solstices. The plasmopause will move toward the Earth as the geomagnetic activity changes from quiet to disturbed. Such variability of the plasmopause has been revealed in numerous observational studies [e.g., Carpenter and Anderson, 1992; Sandel et al., 2003; Spasojević et al., 2003; He et al., 2016, and references therein] and modeling investigations [e.g., Rasmussen et al., 1993; Lambour et al., 1997; Ober et al., 1997; Liemohn et al., 2004].

### 3.4. Solar Cycle Variations

Figure 13 shows the solar cycle variation of the plasmopause locations. The plasmopause locations are first binned into a year-MLT coordinate frame in 1 year and 1 h intervals, respectively, and then plotted in Figure 13. The most important result in Figure 13 is that the plasmopause locations are strongly correlated with solar activity. The plasmopause is significantly negatively correlated to solar activity as represented by the sunspot number. The correlations before 1988 are not so significant as those after 1989, possibly because the number of plasmopause crossings in our database is small before 1988 as indicated in Figure 7. It is also interesting that the plasmopause radial position increases as the peak in solar activity falls from solar cycle 21 to solar cycle 24 as shown in Figure 13 (top). This implies that solar activity plays an important role in the dynamics of the plasmasphere, and the solar cycle effects should be considered in the construction of an empirical plasmopause model.

## 4. Summary and Conclusion

In this paper, we have compiled a large plasmopause location database, based on which the variations of the plasmopause are statistically investigated. The results are summarized as follows:

1. Based on the plasmopause identification criteria for plasma wave instruments and EUV images, a database that contains 49,119 plasmopause crossing events from in situ observations and 3957 plasmopause profiles (corresponding to 48,899 plasmopause locations in 1 h MLT intervals) from remote observations has been assembled, based on data from 18 satellites that cover a period from November 1977 to December 2015. To our knowledge, this is the largest plasmopause database that has so far been developed. This database also contains the matched geomagnetic indices ( $K_p$ ,  $Dst$ , and  $AE$ ) and time-shifted solar wind and IMF parameters ( $V_{SW}$ ,  $N_{SW}$ , and IMF  $B_y$  and  $B_z$ ). This will be an important database for the space research community in investigating inner magnetospheric dynamics associated with other modeling and observations.
2. The responses of the global plasmopause to geomagnetic indices and solar wind changes and the diurnal, seasonal, and solar cycle variations of the plasmopause are investigated based on this database. It is found that the plasmopause shrinks toward the Earth globally and a clear bulge appears in the afternoon to premidnight MLT sector as the solar wind and geomagnetic conditions change from quiet to disturbed. The bulges are clearer during storm times or southward IMF. For the diurnal, seasonal, and solar cycle variations, the  $t$  test indicates that the peaks and valleys in Figures 11–13 are significantly different with 99% confidence levels.
3. The diurnal variations of the plasmopause azimuthal shape are most probably the result of the difference between the magnetic dipole tilt and the Earth's spin axis.
4. The seasonal variation of the plasmopause is characterized by spring and fall valleys and summer and winter peaks.
5. The plasmopause approaches the Earth during high solar activity and expands outward during low solar activity.

Based on this large database and the above mentioned statistical results, a new solar wind-driven global dynamic plasmopause model will be constructed and validated in the companion paper [He et al., 2017].

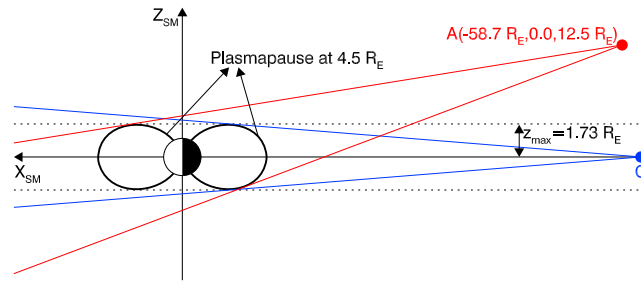


**Figure A1.** Illustration of the LOS configurations for different imaging positions in noon-midnight meridian plane in the SM coordinate system.

This database will also help us to better understand the evolving properties of the plasmapause shape and position as the plasmasphere interacts with the ring current and the radiation belts in the magnetosphere.

## Appendix A: MLA

Determination of the magnetic equatorial plane plasmapause from plasmaspheric EUV images

obtained from side perspectives is challenging. The magnetic dipole nature of the plasmasphere can enable determination of the equatorial plasmapause from just one EUV image even when it is projected on the meridian plane. It is easy to understand the application of the MLA to images from polar perspectives (e.g., IMAGE EUV) since the images are approximately projected onto the magnetic equator (ME) on which the MLT dependencies are apparently exhibited and the MLT dependencies of the plasmapause locations can be determined [Wang *et al.*, 2007]. For side perspectives (e.g., CE 3 EUVC), as is stated in He *et al.* [2011, 2016], there are mainly two limitations in determination of the MLT dependencies of the plasmapause shape from Moon-based images.

The first limitation is the imager-to-ME distance. Taking a plasmasphere with a uniform MLT distribution and plasmapause location at  $L = 4.5 R_E$  for an example, and adopting a dipolar approximation (see Figure A1), the equation for the plasmapause shape is  $r = L \times \cos^2(\theta) = 4.5 \times \cos^2(\theta)$ , where  $\theta$  is latitude in SM and  $r$  is the radial distance of the plasmapause at  $\theta$ . The maximum distance of the plasmapause to the ME can be calculated as  $z_{\max} = L \times \cos^2(\theta) \times \sin(\theta) = 1.73 R_E$ . If the imager-to-ME distance is less than  $z_{\max}$  (e.g., point C in the region confined by the two horizontal dashed lines in Figure A1), then the blue LOS' though pixels on the plasmasphere outline boundary in the images can only be tangent to the plasmapause surface that faces the imager with the other side shaded by the main body of the plasmasphere. For all the cases used in the investigation, the imager-to-ME distance is significantly greater than  $z_{\max}$  (e.g., point A in Figure A1), so the plasmasphere outline boundary can cover all the MLT sectors. Figure A1 is just an example on the noon-midnight meridian plane. For other meridian planes, the principle is the same.

The second limitation is the shading of the main body of the plasmasphere. Due to the observing geometry from a side perspective, the plasmaspheric structures (plume, notch, shoulder, etc.) may be shaded by the main plasmasphere, and only the plasmapause of the main plasmasphere can be determined. In this investigation, only the images with clear and sharp plasmasphere outline boundaries are selected to determine the plasmapause locations on the equatorial plane in SM.

A graphical user interface (GUI) in Interactive Data Language (IDL) is prepared as supporting information Software S1 to show the feasibility of determining the MLT dependence of the plasmapause locations from Moon-based EUV images. In the GUI, the location of the virtual imager is the same as point A in Figure A1. As pointed above, when the imager-to-ME distance is large enough, the LOS' calculated from the pixels on the plasmapause outline boundary in the images can be tangent to the plasmapause surface at all MLTs except for shading of the main plasmasphere.

## References

- Anderson, R. R., D. A. Gurnett, and D. L. Odem (1992), CRRES plasma wave experiment, *J. Spacecr. Rocket.*, 29(4), 570–573, doi:10.2514/3.25501.
- Angelopoulos, V. (2008), The THEMIS mission, *Space Sci. Rev.*, 141, 5–34, doi:10.1007/s11214-008-9336-1.
- Bandić, M., G. Verbanac, M. B. Moldwin, V. Pierrard, and G. Piredda (2016), MLT dependence in the relationship between plasmapause, solar wind, and geomagnetic activity based on CRRES: 1990–1991, *J. Geophys. Res. Space Physics*, 121, 4397–4408, doi:10.1002/2015JA022278.
- Bonnell, J. W., F. S. Mozer, G. T. Delory, A. J. Hull, R. E. Ergun, C. M. Cully, V. Angelopoulos, and P. R. Harvey (2008), The Electric Field Instrument (EFI) for THEMIS, *Space Sci. Rev.*, 141, 303–341, doi:10.1007/s11214-008-9469-2.
- Burch, J. L. (2000), IMAGE mission overview, *Space Sci. Rev.*, 91(1), 1–14, doi:10.1023/A:1005245323115.

### Acknowledgments

The authors sincerely thank the National Astronomical Observatories, Chinese Academy of Sciences, for provision of the CE 3 EUVC data; NASA/CDAWEB for provision of the ISEE 1 PWI data, DE 1 PWI data, Polar PWI data, and IMAGE RPI data; ESA/Cluster Science Archive for provision of the Cluster WHISPER data; Iowa University for the provision of the VAP EMFISIS data available from <http://emfisis.physics.uiowa.edu/data/index>; the THEMIS team for provision of the THEMIS ESA and EFI data available from <http://themis.ssl.berkeley.edu/index.shtml>; JAXA/DARTS for provision of the Akebono PWS data; and T. Forrester of IMAGE EUV team for provision of the IMAGE EUV data and relevant processing software. The authors give thanks to NASA-CCMC for providing the code of IGRF and Tsyganenko model; NASA/GSFC OMNIWeb for providing the 5 min averaged solar wind and IMF data; the Kyoto World Data Center for providing *Dst*, *SYM-H* and *AE*; and the German Research Centre for Geosciences (GFZ) for providing *Kp*. This work was supported by National Natural Science Foundation of China (41274147 and 41674155) and the Youth Innovation Promotion Association of the Chinese Academy of Sciences (2017258). Support for the U.S. authors was provided by NASA. The newly compiled plasmapause database is available by request through email to the corresponding author.



- Burch, J. L., J. Goldstein, and B. R. Sandel (2004), Cause of plasmasphere corotation lag, *Geophys. Res. Lett.*, *31*, L05802, doi:10.1029/2003GL019164.
- Carpenter, D. L. (1963), Whistler evidence of a 'knee' in the magnetospheric ionization density profile, *J. Geophys. Res.*, *68*(6), 1675–1682, doi:10.1029/JZ068i006p01675.
- Carpenter, D. L. (1966), Whistler studies of the plasmopause in the magnetosphere: 1. Temporal variations in the position of the knee and some evidence on plasma motions near the knee, *J. Geophys. Res.*, *71*(3), 693–709, doi:10.1029/JZ071i003p00693.
- Carpenter, D. L. (1995), Earth's plasmasphere awaits rediscovery, *Eos. Trans. AGU*, *76*(9), 89–92, doi:10.1029/95EO00041.
- Carpenter, D. L. (2004), Remote sensing the Earth's plasmasphere, *Rad. Sci. Bull.*, *308*, 13–29.
- Carpenter, D. L., and R. R. Anderson (1992), An ISEE/whistler model of equatorial electron density in the magnetosphere, *J. Geophys. Res.*, *97*(A2), 1097–1108, doi:10.1029/91JA01548.
- Carpenter, L. D., and C. Park (1973), On what ionospheric workers should know about the plasmopause-plasmasphere, *Rev. Geophys. Space Phys.*, *11*, 133–154, doi:10.1029/RG011i001p00133.
- Chao, J. K., D. J. Wu, C.-H. Lin, Y. H. Yang, X. Y. Wang, M. Kessel, S. H. Chen, and R. P. Lepping (2002), Models for the size and shape of the Earth's magnetopause and bow shock, in *Space Weather Study Using Multipoint Techniques, COSPAR Colloq. Ser.*, vol. 12, edited by L.-H. Lyu, pp. 127–134, Oxford, Pergamon, Turkey.
- Chappell, C. R., K. K. Harris, and G. W. Sharp (1970), A study of the influence of magnetic activity on the location of the plasmopause as measured by OGO 5, *J. Geophys. Res.*, *75*(1), 50–56, doi:10.1029/JA075i001p00050.
- Chen, A. J., and R. A. Wolf (1972), Effects on the plasmasphere of a time varying convection electric field, *Planet. Space Sci.*, *20*(4), 483–509, doi:10.1016/0032-0633(72)90080-3.
- Chen, B., et al. (2014), Investigation and calibration of the Moon-based EUV camera for Chang'E-3, *Res. Astron. Astrophys.*, *14*(12), 1654–1663, doi:10.1088/1674-4527/14/12/013.
- Cho, J., D.-Y. Lee, J.-H. Kim, D.-K. Shin, K.-C. Kim, and D. Turner (2015), New model fit functions of the plasmopause location determined using THEMIS observations during the ascending phase of solar cycle 24, *J. Geophys. Res. Space Physics*, *120*, 2877–2889, doi:10.1002/2015JA021030.
- Comfort, R. H., J. H. Waite Jr., and C. R. Chappell (1985), Thermal ion temperatures from the retarding ion mass spectrometer on DE 1, *J. Geophys. Res.*, *90*(A4), 3475–3486, doi:10.1029/JA090iA04p03475.
- Darrrouzet, F., P. M. E. Décréau, and J. Lemaire (2002), The Cluster mission preliminary results obtained with the WHISPER experiment, *Physica Mag.*, *24*, 3–16, doi:10.1.1.568.6231.
- Darrrouzet, F., et al. (2004), Density structures inside the plasmasphere: Cluster observations, *Ann. Geophys.*, *22*, 2577–2585, doi:10.5194/angeo-22-2577-2004.
- Darrrouzet, F., J. De Keyser, P. M. E. Décréau, F. El Lemdani-Mazouz, and X. Vallières (2008), Statistical analysis of plasmaspheric plumes with Cluster/WHISPER observations, *Ann. Geophys.*, *26*, 2403–2417, doi:10.5194/angeo-26-2403-2008.
- Darrrouzet, F., J. De Keyser, and V. Pierrard (Eds.) (2009), *The Earth's Plasmasphere: A Cluster and IMAGE Perspective*, pp. 55–106, Springer, New York, doi:10.1007/978-1-4419-1323-4.
- Darrrouzet, F., V. Pierrard, S. Benck, G. Lointier, J. Cabrera, K. Borremans, N. Y. Ganushkina, and J. De Keyser (2013), Links between the plasmopause and the radiation belt boundaries as observed by the instruments CIS, RAPID and WHISPER onboard Cluster, *J. Geophys. Res. Space Physics*, *118*, 4176–4188, doi:10.1002/jgra.50239.
- Décréau, P. M. E., P. Ferreau, V. Krannosels'kikh, M. Lévêque, P. Martin, O. Randriamboarison, F. X. Sené, J. G. Trotignon, P. Canu, and P. B. Mögensen (1997), WHISPER, a resonance sounder and wave analyser: Performances and perspectives for the Cluster mission, *Space Sci. Rev.*, *79*(157), 193, doi:10.1023/A:1004931326404.
- Fok, M.-C., T. E. Moore, J. U. Kozyra, G. C. Ho, and D. C. Hamilton (1995), Three-dimensional ring current decay model, *J. Geophys. Res.*, *100*(A6), 9619–9632, doi:10.1029/94JA03029.
- Gallagher, D. L., and R. H. Comfort (2016), Unsolved problems in plasmasphere refilling, *J. Geophys. Res. Space Physics*, *121*, 1447–1451, doi:10.1002/2015JA022279.
- Gallagher, D. L., M. L. Adrian, and M. W. Liemohn (2005), Origin and evolution of deep plasmaspheric notches, *J. Geophys. Res.*, *110*, A09201, doi:10.1029/2004JA010906.
- Ganguli, G., M. A. Reynolds, and M. W. Liemohn (2000), The plasmasphere and advances in plasmaspheric research, *J. Atmos. Sol. Terr. Phys.*, *62*(17–18), 1647–1657, doi:10.1016/S1364-6826(00)00117-6.
- Goldstein, J. (2006), Plasmasphere response: Tutorial and review of recent imaging results, *Space Sci. Rev.*, *124*, 203–216, doi:10.1007/s11214-006-9105-y.
- Goldstein, J., M. Spasojevic, P. H. Reiff, B. R. Sandel, W. T. Forrester, D. L. Gallagher, and B. W. Reinisch (2003a), Identifying the plasmopause in IMAGE EUV data using IMAGE RPI in situ steep density gradients, *J. Geophys. Res.*, *108*(A4), 1147, doi:10.1029/2002JA009475.
- Goldstein, J., B. R. Sandel, W. T. Forrester, and P. H. Reiff (2003b), IMF-driven plasmasphere erosion of 10 July 2000, *Geophys. Res. Lett.*, *30*(3), 1146, doi:10.1029/2002GL016478.
- Goldstein, J., B. R. Sandel, W. T. Forrester, M. F. Thomsen, and M. R. Hairston (2005), Global plasmasphere evolution 22–23 April 2001, *J. Geophys. Res.*, *110*, A12218, doi:10.1029/2005JA011282.
- Goldstein, J., S. De Pascuale, C. Kletzing, W. Kurth, K. J. Genestreti, R. M. Skoug, B. A. Larsen, L. M. Kistler, C. Mouikis, and H. Spence (2014), Simulation of Van Allen Probes plasmopause encounters, *J. Geophys. Res. Space Physics*, *119*, 7464–7484, doi:10.1002/2014JA020252.
- Grebowsky, J. M. (1970), Model study of plasmopause motion, *J. Geophys. Res.*, *75*, 4329–4333, doi:10.1029/JA075i022p04329.
- Gringauz, K. I. (1963), The structure of the ionized gas envelope of Earth from direct measurements in the USSR of local charged particle concentrations, *Planet. Space Sci.*, *11*(3), 281–296, doi:10.1016/0032-0633(63)90030-8.
- Gurnett, D. A., and U. S. Inan (1988), Plasma wave observations with the Dynamics Explorer 1 spacecraft, *Rev. Geophys.*, *26*(2), 285–316, doi:10.1029/RG026i002p00285.
- Gurnett, D. A., F. L. Scarf, R. W. Fredricks, and E. J. Smith (1978), The ISEE-1 and ISEE-2 plasma wave investigation, *Trans. IEEE Geosci. Electron.*, *GE-16*(3), 225–230, doi:10.1109/TGE.1978.294552.
- Gurnett, D. A., et al. (1995), The Polar plasma wave instrument, *Space Sci. Rev.*, *71*(1), 597–622, doi:10.1007/BF00751343.
- Harris, K. K., and G. W. Sharp (1969), OGO-V ion spectrometer, *Trans. IEEE Geosci. Electron.*, *GE-7*(2), 93–98, doi:10.1109/TGE.1969.271328.
- Harris, K. K., G. W. Sharp, and C. R. Chappell (1970), Observations of the plasmopause from OGO 5, *J. Geophys. Res.*, *75*(1), 219–224, doi:10.1029/JA075i001p00219.
- Harvey, P., et al. (1995), The electric field instrument on the Polar satellite, *Space Sci. Rev.*, *71*, 583–596, doi:10.1007/BF00751342.
- He, F., X. X. Zhang, B. Chen, and M.-C. Fok (2011), Reconstruction of the plasmasphere from Moon-based EUV images, *J. Geophys. Res.*, *116*, A11203, doi:10.1029/2010JA016364.

- He, F., X. X. Zhang, B. Chen, and M.-C. Fok (2012), Inversion of the Earth's plasmaspheric density distribution from EUV images with genetic algorithm, *Chin. J. Geophys.*, *55*(1), 29–35, doi:10.6038/jissn.0001-5733.2012.01.003.
- He, F., X.-X. Zhang, B. Chen, M.-C. Fok, and S. Nakano (2016), Determination of the Earth's plasmopause location from the CE-3 EUV images, *J. Geophys. Res. Space Physics*, *121*, 296–304, doi:10.1002/2015JA021863.
- He, F., X.-X. Zhang, R.-L. Lin, M.-C. Fok, R. M. Katus, M. W. Liemohn, D. L. Gallagher, and S. Nakano (2017), A new solar wind-driven global dynamic plasmopause model: 2. Model and validation, *J. Geophys. Res. Space Physics*, *122*, doi:10.1002/2017JA023913, in press.
- Horwitz, J. L., R. H. Comfort, and C. R. Chappell (1990), A statistical characterization of plasmasphere structure and boundary locations [J], *J. Geophys. Res.*, *95*, 7937–7947, doi:10.1029/JA095iA06p07937.
- Katus, R. M., D. L. Gallagher, M. W. Liemohn, A. M. Keesee, and L. K. Sarno-Smith (2015), Statistical storm time examination of MLT-dependent plasmopause location derived from IMAGE EUV, *J. Geophys. Res. Space Physics*, *120*, 5545–5559, doi:10.1002/2015JA021225.
- Khazanov, G. V., and M. W. Liemohn (1995), Nonsteady state ionosphere-plasmasphere coupling of superthermal electrons, *J. Geophys. Res.*, *100*(A6), 9669–9681, doi:10.1029/95JA00526.
- Kim, K.-H., F. S. Mozer, D.-H. Lee, and H. Jin (2010), Large electric field at the nightside plasmopause observed by the Polar spacecraft, *J. Geophys. Res.*, *115*, A07219, doi:10.1029/2010JA015439.
- Kletzing, C. A., et al. (2013), The Electric and Magnetic Field Instrument Suite and Integrated Science (EMFISIS) on RBSP, *Space Sci. Rev.*, *179*, 127–181, doi:10.1007/s11214-013-9993-6.
- Kotova, G. A. (2007), The Earth's plasmasphere: Status of studies, *Geomagn. Aeron.*, *47*(4), 409–422, doi:10.1134/S0016793207040019.
- Kurth, W. S., S. De Pascuale, J. B. Faden, C. A. Kletzing, G. B. Hospodarsky, S. Thaller, and J. R. Wygant (2015), Electron densities inferred from plasma wave spectra obtained by the Waves instrument on Van Allen Probes, *J. Geophys. Res. Space Physics*, *120*, 904–914, doi:10.1002/2014JA020857.
- Kwon, H.-J., K.-H. Kim, G. Jee, J.-S. Park, H. Jin, and Y. Nishimura (2015), Plasmopause location under quiet geomagnetic conditions ( $Kp \leq 1$ ): THEMIS observations, *Geophys. Res. Lett.*, *42*, 7303–7310, doi:10.1002/2015GL066090.
- Lambour, R. L., L. A. Weiss, R. C. Elphic, and M. F. Thomsen (1997), Global modeling of the plasmasphere following storm sudden commencements, *J. Geophys. Res.*, *102*(A11), 24351–24368, doi:10.1029/97JA02037.
- Larsen, B. A., D. M. Klumpp, and C. Gurgiolo (2007), Correlation between plasmopause position and solar wind parameter, *J. Atmos. Sol. Terr. Phys.*, *69*, 334–340, doi:10.1016/j.jastp.2006.06.017.
- Lawrence, D. J., M. F. Thomsen, J. E. Borovsky, and D. J. McComas (1999), Measurements of early and late time plasmaspheric refilling as observed from geosynchronous orbit, *J. Geophys. Res.*, *104*, 14,691–14,704, doi:10.1029/1998JA900087.
- Lemaire, J. F., and K. I. Gringauz (1998), *The Earth's Plasmasphere, With Contributions From D. L. Carpenter and V. Bassolo*, pp. 1–14, Cambridge Univ. Press, New York, doi:10.1017/CBO9780511600098.
- Li, W., R. M. Thorne, J. Bortnik, Y. Nishimura, V. Angelopoulos, L. Chen, J. P. McFadden, and J. W. Bonnell (2010), Global distributions of suprathermal electrons observed on THEMIS and potential mechanisms for access into the plasmasphere, *J. Geophys. Res.*, *115*, A00J10, doi:10.1029/2010JA015687.
- Liemohn, M. W. (2006), Introduction to the special section on “Results of the National Science Foundation Geospace Environment Modeling Inner Magnetosphere/Storms Assessment Challenge”, *J. Geophys. Res.*, *111*, A11S01, doi:10.1029/2006JA011970.
- Liemohn, M. W., A. J. Ridley, D. L. Gallagher, D. M. Ober, and J. U. Kozyra (2004), Dependence of plasmaspheric morphology on the electric field description during the recovery phase of the 17 April 2002 magnetic storm, *J. Geophys. Res.*, *109*, A03209, doi:10.1029/2003JA010304.
- Lin, R. L., X. X. Zhang, S. Q. Liu, Y. L. Wang, and J. C. Gong (2010), A three-dimensional asymmetric magnetopause model, *J. Geophys. Res.*, *115*, A04207, doi:10.1029/2009JA014235.
- Liu, X., W. Liu, J. B. Cao, H. S. Fu, J. Yu, and X. Li (2015), Dynamic plasmopause model based on THEMIS measurements, *J. Geophys. Res. Space Physics*, *120*, 10,543–10,556, doi:10.1002/2015JA021801.
- McFadden, J. P., C. W. Carlson, D. Larson, M. Ludlam, R. Abiad, B. Elliott, P. Turin, M. Marckwordt, and V. Angelopoulos (2008), The THEMIS ESA plasma instrument and in-flight calibration, *Space Sci. Rev.*, *141*, 277–302, doi:10.1007/s11214-008-9440-2.
- Menk, F. W., S. T. Ables, R. S. Grew, M. A. Clilverd, and B. R. Sandel (2012), The annual and longitudinal variations in plasmaspheric ion density, *J. Geophys. Res.*, *117*, A03215, doi:10.1029/2011JA017071.
- Moldwin, M. B., M. F. Thomsen, S. J. Bame, D. J. McComas, and G. D. Reeves (1995), The fine-scale structure of the outer plasmasphere, *J. Geophys. Res.*, *100*, 8021–8029, doi:10.1029/94JA03342.
- Moldwin, M. B., L. Downward, H. K. Rassoul, R. Amin, and R. R. Anderson (2002), A new model of the location of the plasmopause: CRRES results, *J. Geophys. Res.*, *107*(A11), 1339, doi:10.1029/2001JA009211.
- Mozer, F. S. (1973), Analyses of techniques for measuring DC and AC electric fields in the magnetosphere, *Space Sci. Rev.*, *14*(2), 272–313, doi:10.1007/BF02432099.
- Newberry, I. T., R. H. Comfort, P. G. Richards, and C. R. Chappell (1989), Thermal  $\text{He}^+$  in the plasmasphere: Comparison of observations with numerical calculations, *J. Geophys. Res.*, *94*(A11), 15265–15276, doi:10.1029/JA094iA11p15265.
- Ober, D. M., J. L. Horwitz, and D. L. Gallagher (1997), Formation of density troughs embedded in the outer plasmasphere by subauroral ion drift events, *J. Geophys. Res.*, *102*, 14,595–14,602, doi:10.1029/97JA01046.
- O'Brien, T. P., and M. B. Moldwin (2003), Empirical plasmopause models from magnetic indices, *Geophys. Res. Lett.*, *30*(4), 1152, doi:10.1029/2002GL016007.
- Ogilvie, K. W., T. von Rosenvinge, and A. C. Dungey (1977), International Sun-Earth Explorer: A three-spacecraft program, *Science*, *198* (4313), 131–138, doi:10.1126/science.198.4313.131.
- Olsen, R. C., S. D. Shawhan, D. L. Gallagher, J. L. Green, C. R. Chappell, and R. R. Anderson (1987), Plasma observations at the Earth's magnetic equator, *J. Geophys. Res.*, *92*(A3), 2385–2407, doi:10.1029/JA092iA03p02385.
- Oya, H., A. Morioka, K. Kobayashi, M. Iizima, T. Ono, H. Miyaoka, T. Okada, and T. Obara (1990), Plasma wave observation and sounder experiments (PWS) using the Akebono (EXOS-D) satellite—Instrumentation and initial results including discovery of the high altitude equatorial plasma turbulence, *J. Geomagn. Geoelectr.*, *42*, 411–442, doi:10.5636/jgg.42.411.
- Pedersen, A., F. Mozer, and G. Gustafsson (1998), Electric field measurements in a tenuous plasma with spherical double probes, in *Measurement Techniques in Space Plasmas: Fields, Geophys. Monogr. Ser.*, vol. 103, edited by R. F. Pfaff, J. E. Borovsky, and D. T. Young, pp. 1–12, AGU, Washington, D. C.
- Pierrard, V., J. Goldstein, N. André, V. K. Jordanova, G. A. Kotova, J. F. Lemaire, M. W. Liemohn, and H. Matsui (2009), Recent progress in physics-based models of the plasmasphere, *Space Sci. Rev.*, *145*, 193–229, doi:10.1007/s11214-008-9480-7.
- Rasmussen, C. E., S. M. Guitart, and S. G. Thomas (1993), A two-dimensional model of the plasmasphere: Refilling time constant, *Planet. Space Sci.*, *41*(1), 35–43, doi:10.1016/0032-0633(93)90015-T.

- Reinisch, B. W., et al. (2000), The Radio Plasma Imager investigation on the IMAGE spacecraft, *Space Sci. Rev.*, *91*(1), 319–359, doi:10.1023/A:1005252602159.
- Press, W. H., S. A. Teukolsky, W. T. Vetterling, and B. P. Flannery (1992), *Numerical Recipes*, pp. 603–649, Cambridge Univ. Press, Cambridge, U. K.
- Russell, C. T. (2001), Solar wind and interplanetary magnetic field: A tutorial, in *Space Weather*, edited by P. Song, H. J. Singer, and G. L. Siscoe, pp. 73–89, AGU, Washington, D. C., doi:10.1029/GM125p0073.
- Russell, C. T., and R. L. McPherron (1973), Semiannual variation of geomagnetic activity, *J. Geophys. Res.*, *78*(1), 92–108, doi:10.1029/JA078i001p00092.
- Roelof, E. C., and A. J. Skinner (2000), Extraction of ion distributions from magnetospheric ENA and EUV images, *Space Sci. Rev.*, *91*, 437–459, doi:10.1007/978-94-011-4233-5\_15.
- Sandel, B. R., et al. (2000), The Extreme Ultraviolet Imager investigation for the IMAGE mission, *Space Sci. Rev.*, *91*(1), 197–242, doi:10.1023/A:1005263510820.
- Sandel, B. R., J. Goldstein, D. L. Gallagher, and M. Spasojević (2003), Extreme Ultraviolet Imager observations of the structure and dynamics of the plasmasphere, *Space Sci. Rev.*, *109*(1), 25–46, doi:10.1023/B:SPAC.0000007511.47727.5b.
- Sarno-Smith, L. K., M. W. Liemohn, R. M. Skoug, B. A. Larsen, M. B. Moldwin, R. M. Katus, and J. R. Wygant (2016), Local time variations of high-energy plasmaspheric ion pitch angle distributions, *J. Geophys. Res. Space Physics*, *121*, 6234–6244, doi:10.1002/2015JA022301.
- Scudder, J. D., X. Cao, and F. S. Mozer (2000), Photoemission current-spacecraft voltage relation: Key to routine, quantitative low-energy plasma measurements, *J. Geophys. Res.*, *105*, 21,281–21,294, doi:10.1029/1999JA900423.
- Shawhan, S. D., D. A. Gurnett, D. L. Odem, R. A. Helliwell, and C. G. Park (1981), The plasma wave and quasi-static electric field instrument (PWI) for Dynamics Explorer-A, *Space Sci. Instrum.*, *5*, 535–550.
- Sitnov, M. I., N. A. Tsyganenko, A. Y. Ukhorskiy, and P. C. Brandt (2008), Dynamical data-based modeling of the storm-time geomagnetic field with enhanced spatial resolution, *J. Geophys. Res.*, *113*, A07218, doi:10.1029/2007JA013003.
- Spasojević, M., J. Goldstein, D. L. Carpenter, U. S. Inan, B. R. Sandel, M. B. Moldwin, and B. W. Reinisch (2003), Global response of the plasmasphere to a geomagnetic disturbance, *J. Geophys. Res.*, *108*(A9), 1340, doi:10.1029/2003JA009987.
- Tsuruda, K., and H. Oya (1991), Introduction to the EXOS-D (Akebono) project, *Geophys. Res. Lett.*, *18*(2), 293–295, doi:10.1029/91GL00039.
- Tsyganenko, N. A., and M. I. Sitnov (2007), Magnetospheric configurations from a high-resolution data-based magnetic field model, *J. Geophys. Res.*, *112*, A06225, doi:10.1029/2007JA012260.
- Verbanac, G., V. Pierrard, M. Bandić, F. Darrouzet, J.-L. Rauch, and P. M. E. Décréau (2015), The relationship between plasmopause, solar wind and geomagnetic activity between 2007 and 2011, *Ann. Geophys.*, *33*, 1271–1283, doi:10.5194/angeo-33-1271-2015.
- Wang, C., T. S. Newman, and D. L. Gallagher (2006), Synthesis of 3D model of a magnetic field-influenced body from a single image, in *Proc. Third International Symposium on 3D Data Processing, Visualization and Transmission*, pp. 1018–1025, IEEE, Chapel Hill, N. C., doi:10.1109/3DPVT.2006.133.
- Wang, C., T. S. Newman, and D. L. Gallagher (2007), Plasmopause equatorial shape determination via the Minimum L algorithm: Description and evaluation, *J. Geophys. Res.*, *112*, A12201, doi:10.1029/2006JA012202.
- Yoshikawa, I., et al. (2008), Telescope of extreme ultraviolet (TEX) onboard SELENE: Science from the Moon, *Earth Planets Space*, *60*(4), 407–416, doi:10.1186/BF03352805.
- Zhang, X. X., C. Wang, T. Chen, Y. L. Wang, A. Tan, T. S. Wu, G. A. Germany, and W. Wang (2005), Global patterns of Joule heating in the high-latitude ionosphere, *J. Geophys. Res.*, *110*, A12208, doi:10.1029/2005JA011222.